Polymer 50 (2009) 3225–3233

Contents lists available at ScienceDirect

Polymer

journal homepage: www.elsevier.com/locate/polymer

# Characterizing interfacial structure of TPO/CPO/TPO adhesive joints by PFM–AFM and SEM

Kangqing Deng [a,b], Mitchell A. Winnik [a,b,*], Ning Yan [c,**], Zhaohua Jiang [a,**], Philip V. Yaneff [d], Rose A. Ryntz [e]

[a] Department of Applied Chemistry, Harbin Institute of Technology, Harbin 150001, China
[b] Department of Chemistry, University of Toronto, 80 St. George Street, Toronto, Ontario M5S 3H6, Canada
[c] Faculty of Forestry, University of Toronto, 33 Willcocks Street, Toronto, Ontario M5S 3B3, Canada
[d] E.I. DuPont Canada, 408 Fairall Street, Ajax, Ontario, Canada
[e] Visteon Automotive Systems, Dearborn, MI 58121, USA

ARTICLE INFO

*Article history:*
Received 21 February 2009
Received in revised form
18 April 2009
Accepted 24 April 2009
Available online 19 May 2009

*Keywords:*
Polypropylene blends
TPO
Adhesion promoter

ABSTRACT

The influence of annealing and EBR component in injection-molded thermoplastic polyolefin (TPO) plaques on adhesion strength of CPO to TPO was investigated by a lap shear test. The TPO was fabricated as a blend of highly crystalline isotactic polypropylene (iPP) and low crystalline poly(ethylene-butene) impact modifier (EBR28). The CPO was a maleated chlorinated polypropylene containing 21.8 wt% Cl. High resolution pulsed force mode–atomic force microscopy (PFM–AFM) combined with the image analysis was used to characterize the interfacial properties of the lap shear joints. Based on PFM–AFM stiffness images, a "transition zone" with a width on the order of 600–1500 nm was observed between CPO and the TPO substrate that may play an important role in affecting the adhesion strength. This zone exhibits enhanced stiffness after annealing at 120 °C. The PFM–AFM images further show that the interface between iPP and CPO without annealing is very sharp and the interface between TPO and CPO without annealing is wider than the interface between iPP and CPO. Annealing (120 °C/20 min) leads to broadening of the interface between TPO and CPO. The thickness of the interface in lap shear joints was obtained from the *z*-directional line profiles of the stiffness maps. The fracture surface morphology was revealed by scanning electronic microscope (SEM), which showed that the fracture structure varied with both the addition of EBR28 in TPO plaques and the annealing condition. Finally, a correlation of interfacial properties to adhesion was obtained: higher stiffness in the transition zone coupled with a thicker interface resulted in stronger adhesion and cohesive failure within the CPO and TPO. In the case of CPO/iPP, the narrow interface and absence of a clearly defined transition zone correlated with interfacial failure between these components.



## 1. Introduction

Thermoplastic olefins (TPOs) are a family of blends that consist of isotactic polypropylene (iPP) with various other polyolefins, such as ethylene copolymers with propylene (EPR) or with butene (EBR), as impact modifiers (IM). Because of their light weight, low cost, good mechanical properties and recyclability, and relative ease of molding into complex shapes, they have become an important class of materials for the automotive industry. They are used to make many interior and exterior automotive parts such as bumpers, fenders and fascia, etc. [1]. These automotive parts, particularly those for exterior applications, are usually painted to enhance both longevity and cosmetic appearance [2].

There are two reasons for adding an impact modifier into TPO: one is to enhance the mechanical properties of iPP in the solid state [3]; the other is to promote adhesion between the iPP and the surface paint. Yokoyama and Ricco [4] found that EBR has a higher toughening efficiency than EPR, and the fracture toughness of iPP can be increased by increasing the molecular weight of the impact modifier. But even with the addition of the impact modifier, the surface of TPO is still difficult to paint. The commonly used method to promote the adhesion of TPO to paint is to include an adhesion promoter in the formulation. The adhesion promoter has to have

* Corresponding author. Department of Chemistry, University of Toronto, 80 St. George Street, Toronto, Ontario M5S 3H6, Canada. Tel.: +1 416 978 6495; fax: +1 416 978 0541.
** Corresponding authors.
*E-mail addresses:* mwinnik@chem.utoronto.ca (M.A. Winnik), ning.yan@utoronto.ca (N. Yan), jiangzhaohua@hit.edu.cn (Z. Jiang).

0032-3861/$ – see front matter © 2009 Elsevier Ltd. All rights reserved.
doi:10.1016/j.polymer.2009.04.079

good adhesion to both the TPO surface and to the paint layer. One class of widely used adhesion promoters is the chlorinated polyolefins (CPOs). There are many types of CPOs. The CPOs based on iPP can differ in chain length, chlorine content, and the amount of succinic anhydride groups introduced through maleation. Although CPO has been used in the automotive industry for many years, paint-adhesion failure, which often occurs on curved surfaces, is still a serious problem for the industry. There is still a lack of fundamental understanding of the adhesion mechanism between CPO and TPO.

There have been many studies on the morphology of injection molding TPO plaques. Injection-molded polypropylene TPO plaques have been shown to have a distinctive skin and core structure when their cross sections are observed with a polarizing microscope. The skin layer consists of a highly birefringent region, which is very different from the crystals found in core (bulk) [5]. The skin layer is formed through shear-induced crystallization in the surface region of the mold. The thickness of the skin layer varies widely with the kind of resin and the molding conditions, as well as with the physical properties of the sample, such as the elastic modulus, the yield strength, and the extent of mold shrinkage. Tang [6] found an iPP-rich layer at the TPO surface and a well-elongated fibrous morphology of the rubber components in the iPP matrix located just below the iPP-rich layer. Matsumoto et al. [7] found that the thickness of these oriented layers was governed mainly by resin and mold temperature. Fujiyama and Wakino [8,9] found that the iPP-rich skin layer was about 600 μm thick under their injection molding condition. The skin layer thickness reported by Ryntz et al. [10] ranged from about 240 μm to 460 μm. Pennington et al. [11] used a Photoacoustic Fourier Transform Infrared (PAFT-IR) technique to perform depth profiling 3–50 μm underneath the surface of the injection-molded iPP-EPR TPO samples. They found that the crystalline iPP phase was located approximately 7–9 μm below the TPO surface, while the EPR layer was present at 15 μm and extended to the bulk. Moffitt et al. [12], combined Polarizing Optical Microscopy (POM) with Laser Scanning Confocal Fluorescence Microscopy (LCFM), and identified a "fine-grained layer" of impact modifier in the form of small droplets beneath the skin layer. The skin layer itself consisted of long fibers of EBR trapped by the shear-induced crystallization of iPP. This EBR-rich area was believed to be responsible for the "paintability" of the TPO parts.

Some studies have attempted to characterize the interfacial structure between TPO and CPO. Mirabella and Dioh [13] used scanning transmission X-ray microscopy (STXM) to characterize the TPO/CPO interface and found an interface of $340 \pm 80$ nm in thickness. Recently, Yin et al. [2] used transmission electron microscopy in conjunction with EDX to probe the interfacial structure of CPO/TPO (iPP/EBR9). They found that the interfacial thickness of TPO/CPO is $23 \pm 2$ nm before annealing and the thickness became $28 \pm 1$ nm after annealing at 120 °C for 30 min. When the sample was annealed at 120 °C in the presence of xylene vapor, the interface thickness of TPO/CPO increased to $50 \pm 4$ nm.

The adhesion mechanism by CPO is still under speculation. It has been suggested that the adhesion between CPO and TPO is due to the preferential interaction of CPO with the impact modifier at the TPO surface. Tomasetti et al. [14]. reported that the adhesion of CPO to blends of iPP/EPR was much higher than that of CPO to iPP itself. Ryntz et al. [15–17]. hypothesized that the morphology at or near the TPO surface played a crucial role in determining the strength of the interaction of TPO with the adhesion promoter. They investigated the effect of TPO morphology on subsequent paintability and thermal shock performance of TPO and suggested that the rearrangement of polypropylene crystallites at the uppermost surface of the TPO during a 120 °C annealing step accounts for the increased cohesive strength of the painted TPO composite, and the swelling of the rubber in TPO by solvents contained within topcoats affords the initial adhesion of the paint to TPO. Aoki [18] postulated that the diffusion of CPO molecules through the polypropylene boundaries with subsequent "mechanical interlocking" with the EBR rubber molecules accounted for the adhesion between the paint and the TPO substrate. Morris et al. [19,20] used confocal Raman microscopy to monitor penetration of the CPO into an EPR-iPP TPO substrate and found that CPO penetrated 20 μm in depth into the TPO substrate under their coating and bake conditions.

Some techniques, such as X-ray microfocus fluoroscopy, visible-light differential interference microscopy and photoacoustic Fourier transform infrared spectroscopy [15], have been used to determine the TPO surface morphology. But they have a low spatial resolution (several micrometers). LSCFM has a spatial resolution of 0.5 μm [21]. This scale is also inadequate for probing the interface of TPO and CPO, which is thought to be on the order 50 nm thick. Scanning transmission X-ray microscopy (STXM) has a practical spatial resolution of 50 nm, and has been used to obtain direct images of TPO surface morphology [2,13]. TEM and AFM have a much higher resolution than STXM; however, the practical resolution that one can obtain with these semi-crystalline polyolefin samples will be limited by sample preparation and, for TEM, the sensitivity of the sample to the electron beam.

In order to extend the capabilities of AFM, Marti [22,23] introduced a non-resonant, intermittent-contact operational mode in atomic force microscopy called pulse force mode (PFM). When AFM is driven in "pulsed force mode", the topography, adhesion, and stiffness maps of a surface can be simultaneously obtained. PFM–AFM is especially useful for imaging soft samples such as polymers, biological molecules, and dendrimer molecules [22,24]. PFM–AFM can also be a useful tool to study non-homogeneous surfaces containing many different materials such as polymer blends, composite materials and sticky surfaces [23,25]. For example, Di Risio [26] has successfully developed a method using PFM–AFM to characterize the spatial arrangement of latex binders in the cross sections of paper model coatings applied on plastic films.

The aim of this study was to apply PFM–AFM method to characterize the interfacial structure of CPO/TPO (iPP-EBR28), and to correlate the interfacial structure to the adhesion properties of TPO/CPO/TPO lap shear joints in order to obtain a better understanding of the fracture and adhesion mechanism of TPO/CPO. To achieve these objectives, a lap shear test was used to characterize the adhesion strength of TPO to CPO. SEM was employed to observe the fracture surface structure. PFM–AFM was used to acquire the cross sectional stiffness images of TPO/CPO/TPO lap shear joints. Through image analysis, *z*-directional line and area profile based on the stiffness were constructed; the interface structure and the interface thickness were obtained. Finally, the correlation of the interfacial properties to fracture strength and fracture energy of the lap shear joints was obtained. Moreover, the adhesion promotion mechanism of CPO and fracture mechanism of lap shear joints were proposed.

## 2. Experimental

### 2.1. Materials

TPO samples were fabricated with polymers from ExxonMobil. The isotactic polypropylene (iPP, Escorene 1042, Ziegler Natta catalyst) was melt-blended with poly(ethylene-butene) (EBR28, Exact 4049, 28 wt% butene, metallocene catalyst). According to Ref. [27] and the data from ExxonMobil Chemical, the iPP sample is characterized by the molecular weight ($M_n$) = 67,070 g/mol with polydispersity index (PDI) = 3.51, melt flow index (MI) = 1.9 g/10 min, density ($d$) = 0.9 g/cm$^3$, and the EBR28 by $M_n$ = 68,700 g/mol, MI = 4.5 g/10 min, $d$ = 0.873 g/cm$^3$. The injection-molded TPO

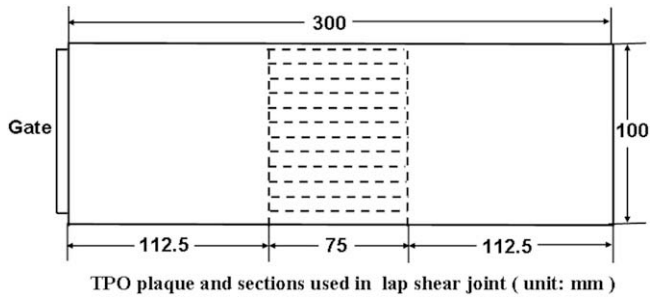


**Fig. 1.** The dimensions of the TPO V-plaques that were provided by Visteon Co. The dashed lines indicate where the plaque was cut to obtain the rectangle sections.

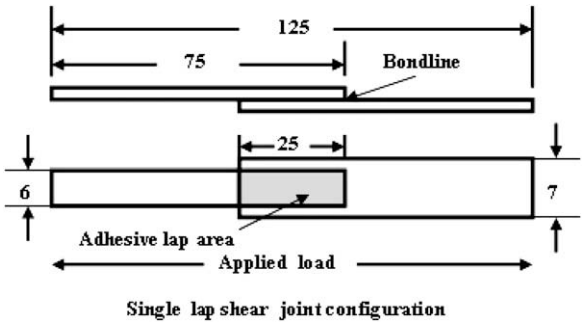


**Fig. 2.** Lap shear joint geometry used in this study.

plaques with dimensions of 300 × 100 × 3 mm$^3$ were provided by Visteon. They were prepared by injection molding through a gate at one end of the mold. The gate width was identical to that of the plaques. In this study, TPO12 refers to an iPP-EBR28 blend containing 12 wt% of EBR28. TPO25 refers to a similar blend containing 25 wt% of EBR28.

The chlorinated polypropylene sample (CPO, Superchlon 872s, 21.8 wt% chlorine content, manufacturer's specification) was provided by Nippon Paper Chemicals Co. Ltd. The molecular weight ($M_n$) of the CPO sample was found to be 29,000 with PDI = 2.9 by gel permeation chromatography (GPC with polystyrene as standards). The melting temperature of CPO is 93.4 °C by differential scanning calorimetry (DSC). An anhydride content of 0.18 mmol/g was found by titration [21]. The CPO samples consisted of a blend of 95 wt% of Superchlon 872 plus 5 wt% of a fluorescent dye-labeled CPO (CPO-HY, 0.1 mmol dye/g polymer) that were prepared previously in this laboratory as a derivative of Superchlon 872 [21].

### 2.2. Single lap shear test

The adhesive strength of TPO to CPO was determined using single lap shear tests. The lap shear joints were made as follows: first, the TPO plaques (provided by Visteon) were cut into sections as shown in Fig. 1. Then, a 10 wt% solution of CPO in tetrahydrofuran (THF) was prepared. THF was used as the solvent in order to minimize the solvent penetration into the polyolefin plaques. After gently cleaning one surface of each iPP or TPO plaque with acetone, the surface was spin-coated with the CPO/THF solution at a speed of 1000 rpm. After drying for 30 min at 50 °C, the coated plaques were baked at 120 °C for 20 min to promote adhesion of CPO to the iPP or TPO substrates. The temperature of 120 °C is above the melting temperature of the EBR28 (55.2 °C, Table 1) in these TPO samples, but well below the normal melting temperature of the iPP matrix (ca. 167.4 °C, Table 1).

**Table 1**
Composition and thermal characteristics of the TPO plaques.

| Sample type | iPP, (wt%) | EBR28, (wt%) | $T_m$[c] (°C) | $\Delta H_m$[c] (J/g) | $\Delta H_m/\Delta H_m^0$[d] |
|---|---|---|---|---|---|
| iPP[a] | 100 | – | 167.4 | 93.9 | 44.9% |
| EBR28[a] | – | 100 | 55.2 | 25.0 | 8.9% |
| TPO12[b] | 88 | 12 | 167.6 | 72.0 | 45.9% |
| | | | 54.8 | 2.0 | 6.0% |
| TPO25[b] | 75 | 25 | 166.8 | 65.4 | 41.7% |
| | | | 47.7 | 7.7 | 10.9% |

[a] iPP, Escorene 1042; EBR28, Exact 4049.
[b] TPO plaques were provided by Visteon.
[c] Thermal data were obtained from DSC measurement under $N_2$ at 10 °C/min from −50 °C to 200 °C.
[d] $\Delta H_{PP}^0 = 209$ J/g, $\Delta H_{PE}^0 = 281$ J/g.

Sandwich-like three-layered samples (iPP/CPO/iPP, or TPO/CPO/TPO) were prepared from pairs of CPO coated plaques. To prepare an individual sample, a pair of CPO coated substrates was placed according to the lap shear geometry in Fig. 2 with the two CPO layers in contact. After that, the lap shear sample was heated at 100 °C for 4 min in a Carver Press under gentle pressure to make sure the central CPO layers were well jointed. The overlap dimensions were 6 mm wide × 25 mm long. Prior to the lap shear tests, the joints were aged for 17 h at 30 °C in a preheated oven. After removal from the oven, they were immediately subjected to shear fracture in the tension mode using an Instron 5543 tester at a crosshead speed of 5 mm/min at room temperature. Force–displacement curves were recorded. At least five specimens of each sample were tested.

### 2.3. Pulsed force mode–atomic force microscopy (PFM–AFM)

#### 2.3.1. Preparation of the cross sections

The iPP/CPO/iPP and TPO/CPO/TPO lap shear joints were sectioned with a razor blade. Then the surface was cryogenically microtomed with freshly prepared glass knives on a Leica (EM FCS) microtome at −60 °C. The thickness of the microtomed sections was 100 nm.

#### 2.3.2. Acquisition of high resolution stiffness maps

High resolution stiffness maps of the cross sections of the TPO/CPO/TPO joints were acquired in air using an Explorer™ SPM modular stage microscope equipped with an external WITec PFM electronics. The force-sensing element was a 450 μm × 50 μm rectangular silicon probe with a nominal spring constant of 0.2 N/m and a nominal resonance frequency of 13 kHz. The following scanning conditions were selected:

- Scan area = 10 μm$^2$ and 50 μm$^2$
- Speed = 5 μm/s for a scan area of 10 μm$^2$, 25 μm/s for a scan area of 50 μm$^2$
- Resolution = 1000 (10 nm/pixel) for a scan area of 10 μm$^2$, 300 (167 nm/pixel) for 50 μm$^2$
- Nominal tip radius <10 nm
- Amplitude = 2.9%
- Frequency = 500 Hz
- Set point = 20 nA
- Ambient conditions = 26 °C (controlled with a temperature stage), RH <40%

#### 2.3.3 Image processing and analysis

The image processing and analysis steps [28] detailed in Table 2 were conducted in SPMLab 6.02, a software included with the AFM device, and in an image analysis program, Image J, developed by

**Table 2**
Image processing and analysis.

| Steps | Process |
|---|---|
| | Stiffness map |
| Image processing | Contrast expansion<br>Common grey level |
| Measurements | *z*-directional profile |

Rasband at the National Institute of Health, USA, which is available in the public domain [29].

### 2.4. Scanning electron microscope (SEM)

The fracture surface morphology of iPP/CPO/iPP and TPO/CPO/TPO lap shear joints were observed with a Hitachi S-5200 scanning electron microscope operated at 1.0–1.5 kV. Fracture surfaces of sections of ca. $3 \times 3 \times 0.4\ mm^3$ in size were examined by SEM.

### 2.5. Differential scanning calorimetry (DSC)

DSC measurements were carried out using a TA Q-100 DSC instrument. It was calibrated with indium, and nitrogen purge gas was employed. Samples of about 8 mg were encapsulated in aluminum pans and heated from −50 °C to 200 °C and then cooled down to −50 °C at a rate of 10 °C/min. After that, the samples were reheated to 200 °C at the same rate.

The enthalpies of crystallization and melting were obtained by integrating the heat flow curve to a flat baseline. The weight fraction of crystallinity $X_c$ was calculated as:

$$X_c = \Delta H_m / \left( f \Delta H_m^0 \right) \quad (1)$$

where, $\Delta H_m$ is the measured enthalpy of melting, $\Delta H_m^0$ is the ideal enthalpy of melting for a perfect crystal of the polymer, and $f$ is the weight fraction of the polymer in the blend. The known $\Delta H_m^0$ value for iPP is 209 J/g and for PE is 281 J/g [30].

## 3. Results

### 3.1. Lap shear test results

From lap shear measurements, both the fracture strength (tensile stress at break) and the adhesion energy $G_c$ were obtained. The adhesion energy $G_c$ is the integrated area under the stress–strain curve. The detailed calculation method for the adhesion energy $G_c$ is presented in Supporting Information.

Initially, we considered only the fracture strength of the three samples, as shown in Fig. 3a. Here one can see that the stress at break for the iPP/CPO sample was smaller than values for the TPO/CPO samples, but the differences were not that large. SEM images of the fracture surfaces (see Fig. 4) showed large differences in the mode of fracture. For the iPP/CPO/iPP sample, interfacial fracture predominated (Fig. 4a), leaving a relatively smooth fracture surface, suggesting weak adhesion. As a consequence, we calculated the adhesion energies for each of the three sets of samples. These results are shown in Fig. 3(b). Here one can see clear differences between the adhesion of CPO to iPP and to TPO. These results lead to the conclusion that the stress at break for the CPO/iPP joint is relatively high, but the adhesion energy is small.

The data in Fig. 3 also show the influence of TPO amount and of annealing at 120 °C on both the stress at break and the fracture energy. Neither factor has much influence on the stress at break. The differences are more pronounced for the fracture energy $G_c$. It appears that annealing above the melting temperature of the EBR component makes the adhesion stronger, but the differences do not lie outside the standard error of our measurements.

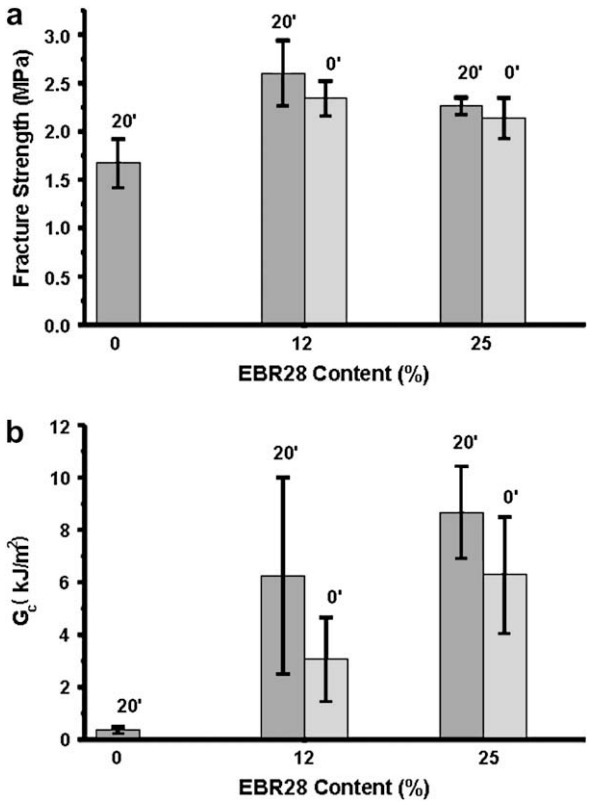


**Fig. 3.** Stress at break and adhesion energy for TPO samples measured by lap shear experiments (a) Fracture strength vs. EBR content in TPO; (b) Adhesion energy vs. EBR content in TPO. 20' indicates that the samples were annealed for 20 min at 120 °C; 0' indicates no annealing.

To put our results in context, both Tomasetti et al. [14] and Yin et al. [31] reported that the adhesion of CPO onto the blends of iPP and EPR was stronger than the adhesion of CPO onto the pure iPP component. Our results are consistent with their findings.

### 3.2. Fracture surface observed by SEM

The fracture surfaces were examined by scanning electron microscopy (SEM) after the joined samples were separated by lap shear tests. Fig. 4a shows a SEM image of iPP/CPO/iPP fracture surface annealed at 120 °C for 20 min. The fracture surface was relatively smooth. Since 120 °C is far below the melting point of iPP, the crystallinity of iPP may have hindered the diffusion of CPO chains into the iPP matrix. As a result, the density of entanglements of iPP and CPO is very small. The mechanism of fracture of iPP/CPO/iPP is likely dominated by chain pullout.

When EBR28 is added to iPP to form TPO25, the fracture mode is greatly changed. Fig. 4b shows the SEM image of a TPO25/CPO/TPO25 fracture surface for a sample subjected to a prebake during sample preparation, but without annealing. One can see that the TPO surface becomes roughened, suggesting that the fracture mode was mixed failure. Because of the good miscibility of EBR with CPO [21], when the lap shear joint is made at 100 °C (above the $T_m$ of EBR28 and CPO), EBR28 and CPO interdiffuse to form the entanglements at the interface. The entanglements at the interface enhance both the fracture strength and fracture energy, which are higher than those of the CPO/iPP joint. In this case, surface roughening is the dominant mechanism for fracture.

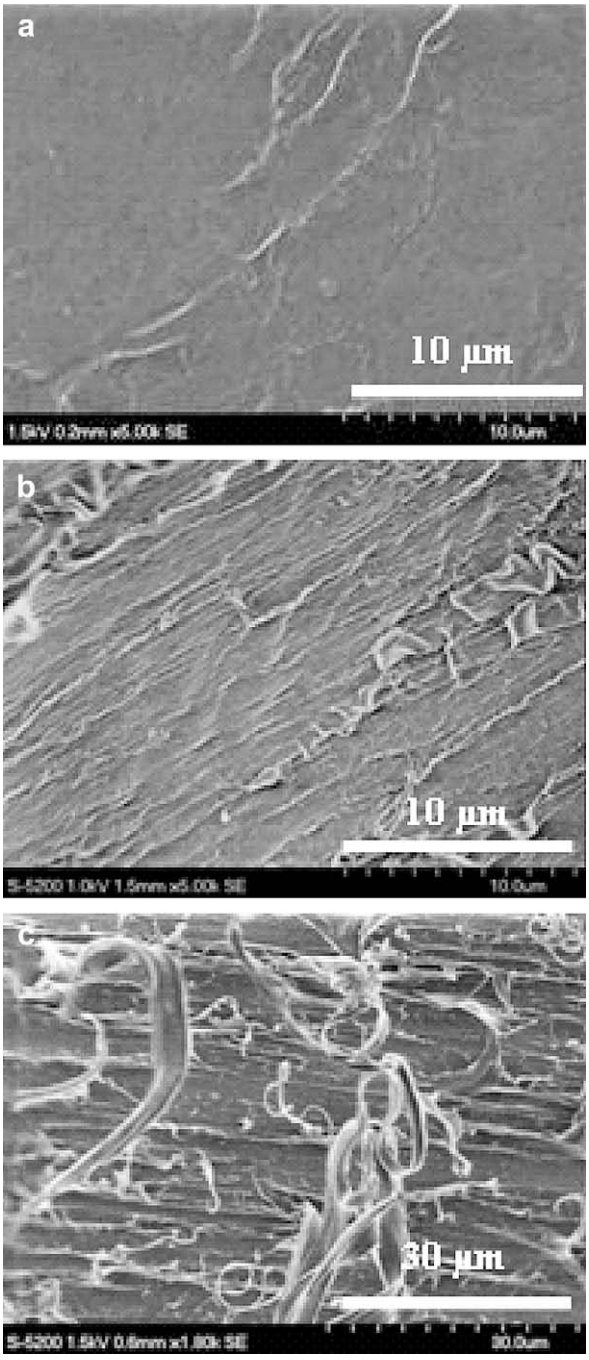


**Fig. 4.** The fracture surfaces of iPP/CPO/iPP and TPO25/CPO/TPO25 lap shear joints. (a) The iPP/CPO/iPP joint, in which the CPO coated PP plaque was annealed at 120 °C for 20 min; (b) the TPO25/CPO/TPO25 joint without annealing; (c) the TPO25/CPO/TPO25 joint, in which the CPO coated TPO plaque was annealed at 120 °C for 20 min.

The image in Fig. 4c shows that when the TPO25/CPO sample was annealed at 120 °C for 20 min, there were significant changes in the fracture mechanism. In addition to surface roughening, one can also see that some TPO fibrils were torn away from the interface. Here it appears that the fracture mode involved cohesive failure. In our view, these phenomena can be attributed to significant interdiffusion of EBR28 and CPO. The fracture mechanism here, which is likely cohesive failure in the TPO and CPO components, leads to surface roughening and fiber formation during failure.

### 3.3. PFM–AFM investigation of the interface region between the substrate and CPO

Like AFM itself, PFM–AFM can provide a convolution-free characterization of topography, adhesion and stiffness properties of a surface. This makes it a powerful tool to study non-homogeneous surfaces of polymer blends. Among the factors that can influence PFM–AFM measurements are water capillary condensation and topography. Water capillary condensation on the sample surface can produce an increased adhesion. In our experiments, during the acquisition of the PFM–AFM stiffness maps, the relative humidity of the environment was kept below RH 40% [26], conditions that are thought to minimize the water capillary condensation effect. Topography can cause artifacts in the stiffness maps due to the variations in contact area between the AFM tip and the sample. In PFM–AFM operations, the topography map is acquired concurrently with the stiffness map. For the lap shear samples involved in these PFM–AFM measurements, 100 nm thick sections were cryomicrotomed at −60 °C, to obtain rather smooth surfaces of the samples. We observed that the stiffness maps have distinctively different morphologies from the topography maps, and high stiffness value regions do not correspond to the high topography regions. As a result, the topography effect was assumed to be minor; and the images were interpreted by assuming that the stiffness variations were associated with the local compositional/structural differences of the surface material.

#### 3.3.1. PFM–AFM measurements at the vicinity of the interface

Fig. 5 shows that differences in stiffness on a μm length scale can be discerned in terms of an area across the interface between the two components. Fig. 5 also illustrates the steps involved in the construction of a *z*-directional area intensity profile. The image shown in Fig. 5a is of a TPO25/CPO/TPO25 sample after annealing at 120 °C for 20 min. First a 10 μm × 10 μm high resolution (10 nm/pixel) stiffness map was acquired. The darker color in Fig. 5a indicates lower stiffness, while the lighter areas represent higher stiffness values. The white rectangle in Fig. 5a defines a region of interest (ROI). After defining a region of interest (ROI), shown by the rectangle, the average stiffness values in the ROI along the z direction were obtained using Image J software (shown in Fig. 5b). Higher intensity value indicates a higher stiffness. Before discussing this result, we first consider the analogous results presented in Fig. 5c and d.

In Fig. 5c, which presents data for a CPO/iPP sample without annealing, one can see that within the vicinity of the interface, there is a drop in stiffness in the CPO domain as one approaches the iPP interface, with a substantial jump in stiffness in the iPP domain itself. In contrast, for the TPO25/CPO/TPO25 sample subjected only to the prebake associated with the sample preparation but not to prolonged annealing (Fig. 5d), there is a region of *reduced* stiffness near the TPO/CPO interface. We do not understand the origin of this effect, which has a width greater than 1 μm, but tentatively refer to it as a transition zone. What is particularly striking in our experiments is that after annealing, the characteristics of the transition zone change. In Fig. 5b, one can see that a somewhat narrower transition zone (ca. 600 nm wide) with a pronounced increase in stiffness was detected by the PFM–AFM probe in the region of the TPO/CPO interface. These values are summarized in Table 3.

#### 3.3.2. PFM–AFM measurements at the interface

In Figs. 6 and 7, we examined PFM–AFM profiles at high resolution and detected stiffness differences from which information about the interface between the two components TPO and CPO could be obtained based on a *z*-directional line profile chosen right at the interface. Fig. 6 illustrates the steps involved in the construction of a *z*-directional line profile from the PFM–AFM images. First

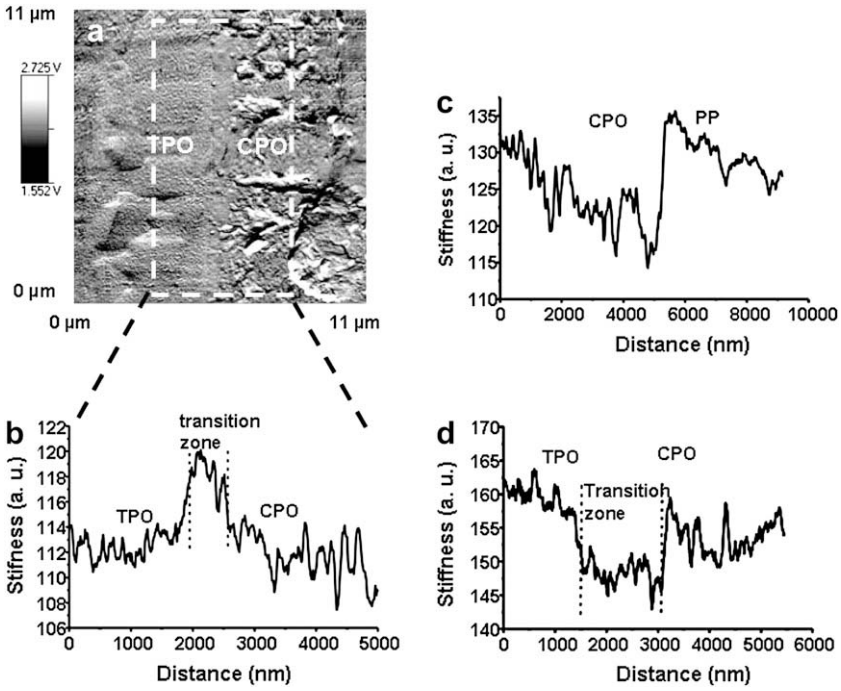


**Fig. 5.** Construction of *z*-directional area profiles from stiffness map of lap shear joints. (a) Stiffness map of TPO25/CPO/TPO25 lap shear joint subjected to a bake at 120 °C/20 min. (b) *z*-directional area profiles from the rectangle in (a); (c) *z*-directional area profile from the stiffness map of an iPP/CPO/iPP lap shear joint without annealing; (d) *z*-directional area profile from the stiffness map of a TPO25/CPO/TPO25 lap shear joint sample without annealing.

a 50 μm × 50 μm low resolution (167 nm/pixel) stiffness map Fig. 6a of the cross section of the lap shear joint sample was acquired to find the interfacial region of TPO/CPO/TPO. Then, a high resolution 10 μm × 10 μm (10 nm/pixel) stiffness map (Fig. 6b) was acquired from scanning the area as indicated by the square in Fig. 6a. After drawing a short horizontal white line perpendicular to the TPO/CPO interface and across the boundary of TPO and CPO layers in Fig. 6b, the difference in stiffness of the surface material along the short white lines was quantified using the imaging analysis software Image J.

Fig. 6a presents the stiffness map of a TPO25/CPO/TPO25 lap shear sample without annealing. We can observe obvious differences in the stiffness between TPO25 and CPO in Fig. 6a. One can also see that the thickness of the CPO layer is about 13 μm. Fig. 6b is the high resolution stiffness map of the region encompassing the interface between TPO25 and CPO. The relative grey scale is such that the high stiffness areas are shown to have brighter grey levels and the low stiffness areas are represented by darker grey levels in the stiffness map. Generally the harder the polymer is, the higher the sample stiffness would be. The higher stiffness of a semi-crystalline polymer also indicates a higher crystallinity. Thus, from this perspective, the stiffness map would show the level of crystallinity of the polymer.

In Fig. 6c, one can see that the intensity of the signal due to stiffness decreases from the TPO phase to the CPO phase. The magnitude of the stiffness signal in the sample is expressed in arbitrary units. The distance scale along the *z*-axis has an arbitrary origin, and the interesting information is the width of the interface determined between the TPO and CPO. We identify the interface in these high magnification images as follows first, two horizontal lines were drawn in the line profile on the two sides of the interface. These represent the average intensity of TPO and CPO near the interface. Then two vertical lines were drawn along the two points of intersection in the line profile corresponding to a sharp change in slope. We interpret the distance between the two vertical lines as the width of the interface. Based on measurements of three line profiles, we obtained an average interface thickness as 28 ± 6 nm from the stiffness map. This value is presented in Table 3.

**Table 3**
The width of transition zone and interface thickness measured from PFM–AFM images.

| Sample | Width of transition zone, nm from stiffness map | Interface thickness[a] (nm) from stiffness map |
|---|---|---|
| iPP/CPO/iPP | Not evident | 21 ± 3 |
| TPO25/CPO/TPO25 | 1500 | 28 ± 6 |
| TPO25/CPO/TPO25 120 °C, 20 min | 620 | 58 ± 5 |

[a] Based on three *z*-directional profiles across the TPO/CPO interface in an individual stiffness image.

In contrast, the sample subjected to annealing appears to have a much broader interface, as shown in Fig. 7. Fig. 7a presents a high resolution (10 nm/pixel) stiffness map of the interface for a TPO25/CPO/TPO25 lap shear sample subjected to annealing (120 °C, 20 min). In Fig. 7b, it can be seen that the intensity of the signal due to stiffness increases from the TPO phase to the CPO phase, which is opposite to that in TPO25/CPO/TPO25 lap shear joint without annealing. However, the interface thickness broadened significantly, from 28 ± 6 nm for the TPO/CPO interface without annealing to 58 ± 5 nm for the TPO/CPO interface subjected to annealing.

In Fig. 8a we present a high resolution stiffness map of an iPP/CPO/iPP lap shear joint without annealing. The interface between the components appears to be very sharp. The *z*-directional profile based on the white line in Fig. 8a is given in Fig. 8b. An interface thickness value of 21 ± 3 nm was obtained from the stiffness map. All of the interface thickness results are presented in Table 3.

These values of the interface thickness for the iPP/CPO interface deduced here can be compared to those reported by Yin et al. [2], from EDX analysis of TEM images, because we used the same iPP and CPO samples as those studied by Yin et al. In those experiments, the authors traced the signal due to Cl atoms across the interface, and obtained signals that were less noisy, and likely more reliable than those obtained here. Our value of 21 ± 3 nm from the stiffness map can be compared to their value of 15 ± 3 nm with reasonably good agreement.

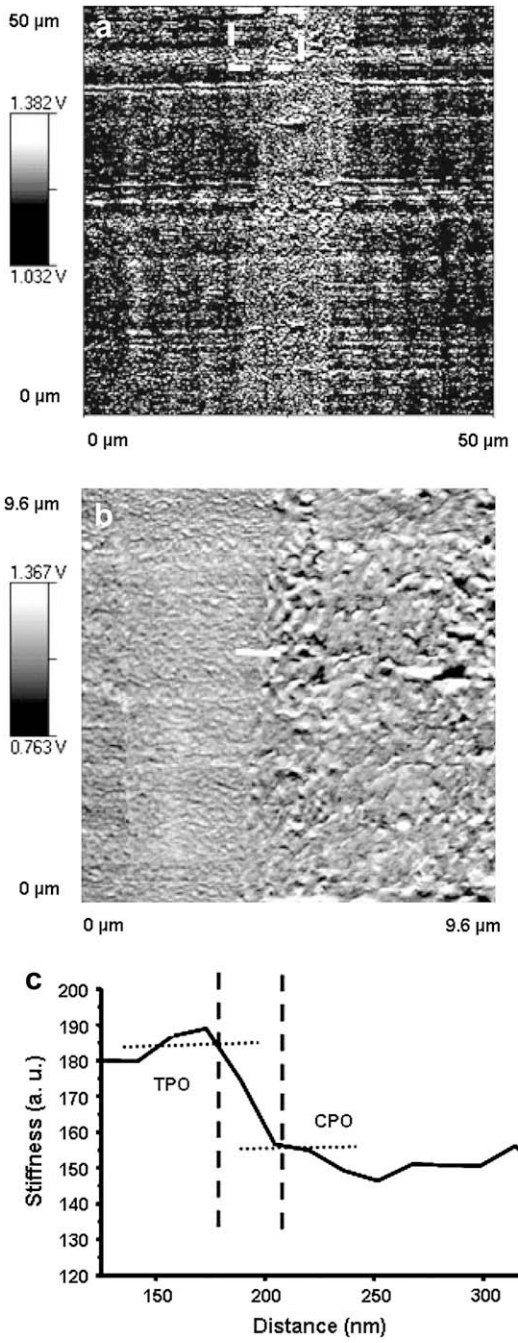


**Fig. 6.** Steps involved in the construction of *z*-directional line profiles used to locate the interface of TPO/CPO in a TPO25/CPO/TPO25 sample without annealing. (a) Stiffness map. (b) Stiffness map from the square region-of-interest in (a). (c) Line intensity profile from the white line in (b). The vertical lines in (c) show the width of the interface.

In contrast, the values we obtain here for the thickness of the TPO/CPO interface for the sample subjected to annealing are much higher than that obtained by Yin et al. ($28 \pm 1$ nm). Here the difference is likely related to the difference in the TPO composition. The experiments reported here employed EBR28 (containing 28 wt% butene), whereas the experiments reported by Yin et al. employed EBR9 (containing only 9 wt% butene). There were also small differences in annealing times (120 °C for 20 min here vs. 120 °C for 30 min for the previous study). These results imply that the composition of the EBR plays an important role in determining the interfacial thickness.

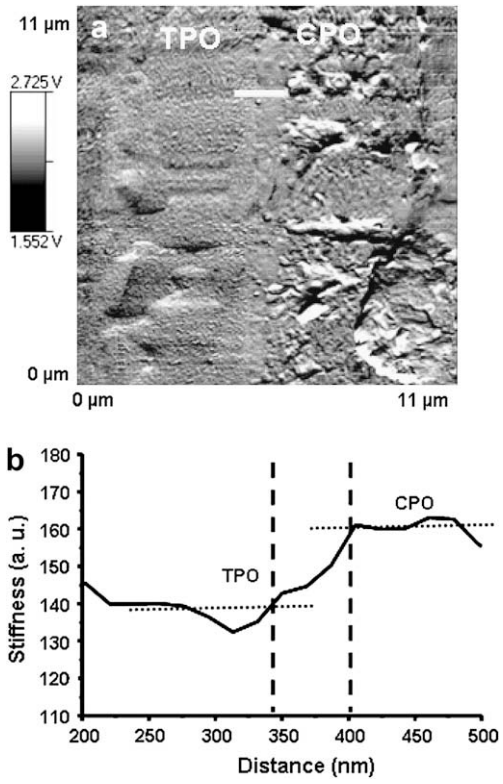


**Fig. 7.** Interface morphology and *z*-directional profiles of TPO25/CPO/TPO25, a lap shear joint subjected to baking at 120 °C for 20 min. (a) Stiffness map; (b) *z*-directional intensity profile from the white line in (a).

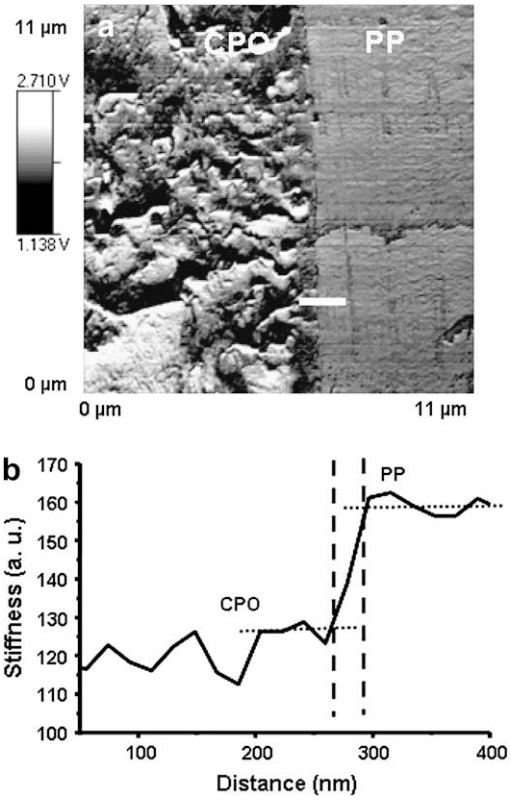


**Fig. 8.** Interface morphology and *z*-directional profiles of iPP/CPO/iPP lap shear joint without annealing. (a) Stiffness map; (b) *z*-directional intensity profile from the white line in (a).

## 4. Discussion

TPO is a blend of two components, isotactic polypropylene (iPP) and an impact modifier; EBR28 in this case is an ethylene–butene copolymer containing 28 wt% butene (EBR28). One of our goals was to compare the interaction of CPO with our TPO sample to that of iPP itself. In order to examine the nature of the interaction of CPO with the TPO and with iPP, we prepared similar iPP/CPO/iPP and TPO/CPO/TPO lap shear joints. We then compared the stress at break and adhesion energy of samples of different compositions and found a striking difference in the adhesion energy of the CPO/TPO joint compared to the CPO/iPP joint, which was much weaker. SEM images of the fracture surfaces also indicated stronger adhesion between TPO and CPO, manifested as substantial crazing during fracture, than in the relatively smooth surfaces seen for CPO/iPP fracture surfaces.

### 4.1. Widths of the interfaces between blend components

Some of the most interesting results came from attempts to measure the width of the interface between CPO and the substrate. Analysis of our PFM–AFM images indicated a width of the iPP/CPO interface of 21 ± 3 nm from the stiffness map. This value is in good agreement with a value of 15 ± 3 nm obtained by Yin et al. by EDX analysis of cryosectioned samples examined by TEM for samples of the same composition under very similar processing conditions. Broader interfaces were found for the TPO/CPO samples. For TPO25/CPO/TPO25 not subjected to annealing, we obtained 28 ± 6 nm for the stiffness map. After annealing, the interface width increased further (58 ± 5 nm). The broadening of the interface between the matrix and CPO supports the idea that when CPO adheres to injection-molded TPO, it interacts more strongly with the impact modifier than with iPP. The annealing temperature was high enough to melt residual crystallinity in the EBR28 domains. This effect in combination with more rapid polymer diffusion at elevated temperature is likely the origin of the broadened interface. The annealing temperature was much below the melting temperature of iPP. One expects little diffusion of CPO into iPP itself or into iPP domains of the TPO. The thinner interface for iPP/CPO joints is consistent with weaker adhesion in these joints.

Ellis [32] tried to understand the origin of the preferential interaction of CPO with TPO compared to iPP in terms of calculated Flory–Huggins interaction parameters. From computed values based on assumed compositions and the Helfand–Tagami relationship, he predicted an interfacial width on the order of 10 nm between iPP and chlorinated PP containing ca. 20 wt% Cl. His analysis is consistent with our finding of a 21 nm thick interface between iPP and a CPO containing 21.8 wt% Cl.

While Yin et al. also noted broadening of the TPO/CPO interface in their system upon annealing, they employed a TPO with a different EBR impact modifier (EBR9, 9 wt% butene). In the sample they examined after annealing at 120 °C for 30 min, they found an interface width of only 28 ± 1 nm. EBR9 is more crystalline and has a higher melting temperature (30%, 107 °C) [2] than EBR28 (8.9%, 55 °C). We can infer that the combination of the chemical composition of the impact modifier, its degree of crystallinity, and the annealing temperature relative to its melting point, affect the degree of interpenetration at the interface of the CPO and EBR molecules.

We also find it gratifying that in comparable systems, the results obtained by PFM–AFM are in reasonable agreement with those obtained by EDX/TEM measurements on similar cryosectioned samples. As we mentioned above, the results of EDX measurements are less noisy and likely to be more reliable than those reported here by PFM–AFM. Nevertheless, EDX measurements can only be used when one component of a blend contains an atom such as chlorine not present in the blend partner. PFM–AFM in this aspect is more general because it measures stiffness changes across an interface irrespective of the chemical composition.

### 4.2. Comparing fracture measurements and PFM–AFM results

While there is clear evidence that the iPP/CPO joint is weaker than that of TPO/CPO, the fracture measurements provide an indication that annealing at 120 °C promotes a stronger bond between CPO and TPO. In these qualitative terms, the fracture strength and adhesion energy have the same trend as the interface thickness. The fracture strength and adhesion energy are measured quantities. They are the quantities of interest in assessing the strength of adhesion of iPP or TPO to CPO. The interface thickness is a representation of thermodynamic quantity that reflects the extent of polymer chain interpenetration across the interfaces between adjacent polymers. The magnitude of the values determined here, and the concordance between these values (for iPP/CPO) and those determine by Yin et al. suggest that these are meaningful values. They are on the order of magnitude of what one would expect for modest to weak miscibility between the components. More troublesome to understand is the "transition zone" seen in Fig. 5. It describes a change in polymer stiffness in the vicinity region of the interface, but on a much longer length scale than the polymer interface itself. For the soft-baked TPO25/CPO/TPO25 sample directly from the Carver press, the transition zone is a region of depressed stiffness. After annealing at 120 °C for 20 min, the transition zone narrows in width and is now

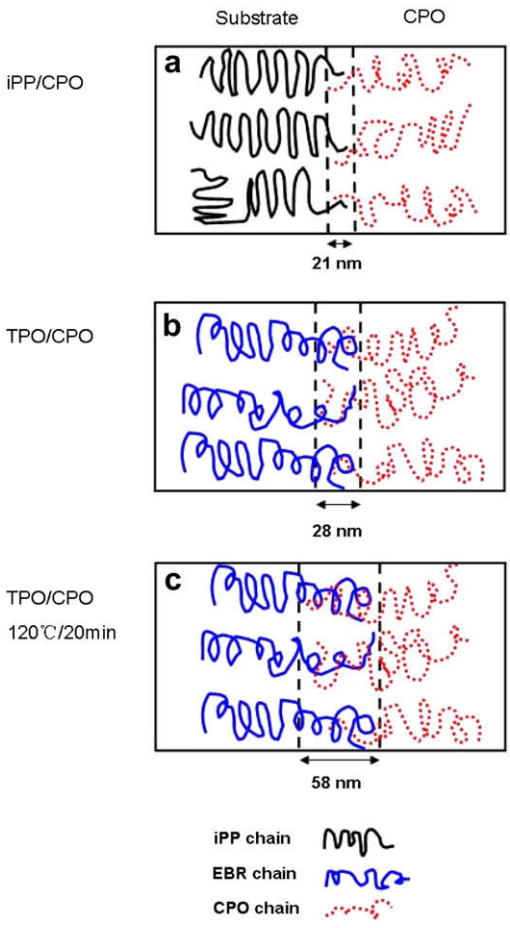


**Fig. 9.** The proposed interfacial adhesion mechanism of CPO to TPO. (a) iPP/CPO sharp interface; (b) Broadened interface of TPO25/CPO without annealing; (c) The widest interface of TPO25/CPO, in which CPO coated TPO plaque was annealed at 120 °C for 20 min.

a region of enhanced stiffness compared to the surrounding components. For *iPP/CPO/iPP*, we do not see a well defined transition zone, but rather a decrease in stiffness adjacent to the iPP/CPO interface. While we do not understand the detailed nature of the transition zone, it appears to play an important role in directing crack propagation during fracture.

Based on the above observations, we hypothesize that when the surface of the pure iPP plaque was coated with CPO, the limited miscibility of the two polymers, as well as the crystallinity of the iPP prevented the CPO macromolecules from diffusing very far into the iPP substrate. This resulted in a sharp interface and weak zone between the CPO and iPP. As a consequence, when subjected to stress, the sample underwent interfacial fracture to yield a smooth surface at the CPO/iPP interface. For the *TPO25/CPO/TPO25* sample under the soft-bake conditions of sample preparation in the Carver press, the CPO was able to diffuse further into the TPO plaque, presumably into EBR domains. This led to a broadened interface region and a stronger transition zone. Here fracture resulted in surface roughening on the fracture surface. When the *TPO25/CPO/TPO25* sample was annealed at a temperature above the melting point of both EBR28 and CPO ($T_m = 92.6\,^{\circ}C$), the EBR and CPO molecules underwent more substantial interdiffusion. This process greatly widened the interface region. After the sample cooled and crystallized, it formed a very stiff transition zone. Thus, baking at 120 °C followed by cooling significantly enhanced the adhesion of CPO to TPO.

In Fig. 9 we present drawings that attempts to describe the molecular factors that promote interfacial adhesion of CPO to TPO. Fig. 9a shows the interfacial structure of a CPO coated iPP plaque. During the preparation of the lap shear joints, the samples are pressed at a temperature of 100 °C, above the melting temperature of CPO but below the melting point of iPP. Little diffusion of CPO into the semi-crystalline iPP takes place, leading to a narrow interface and weak adhesion. Fig. 9b shows the interfacial structure of CPO coated TPO plaque without annealing. During the preparation of the lap shear joints, the sample temperature reaches 100 °C, which is above the melting temperature of both CPO and that of EBR28. For this brief soft bake time, the CPO molecules can penetrate into EBR domains. A broader interface is formed. Note that in Fig. 9b and c, no iPP chains are shown, suggesting that mixing occurs with EBR domains at the substrate surface, and that these domains are larger than the scale of the drawing.

During the annealing step, the annealing temperature 120 °C is well above the melting temperature of CPO and that of EBR. This promotes extensive interdiffusion of CPO and EBR molecules. This results in the widest interface and the strongest adhesion.

## 5. Summary

In this study, the interfacial structure of TPO/CPO/TPO lap shear joints was investigated by high resolution PFM–AFM and compared to the fracture strength of the joint. In addition, the fracture surfaces were examined by SEM. Based on these results, the adhesion and fracture mechanism of TPO/CPO/TPO were discussed.

High resolution PFM–AFM images on thin cryosectioned samples revealed a sharp interface between iPP and CPO (21 nm), and a wider interface (28 nm) between TPO and CPO in a sample prepared by heating briefly to 100 °C. Samples annealed at 120 °C for 20 min (above the melting temperature of both CPO and the EBR impact modifier) showed an even broader interface (ca. 58 nm). These results are in accord with the idea that CPO interacts preferentially with the impact modifier as it promotes adhesion to TPO. We show that the interface for CPO with this EBR sample, with 28 wt% butene, is much broader than that between the same TPO and a more crystalline EBR containing only 9 wt% butene.

SEM images showed a smooth fracture surface for iPP/CPO/iPP samples. Surface roughening was observed in TPO25/CPO/TPO25 fracture surfaces without annealing and both surface roughening and TPO fibrils coexisted on the fracture surfaces of TPO25/CPO/TPO25 subjected to annealing. In addition, fracture properties were found to correlate with the interface structure. A novel observation from the PFM–AFM results was the presence in TPO/CPO samples of a transition zone in the region of the interface, with a width on the order of 600–1500 nm and a significantly different stiffness than the material on either side of it. The origin of this zone is not understood, but its nature appears to affect the nature of the fracture mechanism. Stiffness variations were also seen on a μm length scale within the CPO phase in the vicinity of the CPO/iPP interface, with a sharp increase in stiffness in the iPP phase. This sample underwent interfacial fracture to yield a relatively smooth fracture surface as seen by SEM.

## Acknowledgements

The authors would like to thank Visteon, DuPont Canada, and NSERC Canada for their financial support. We thank Visteon for kindly providing TPO samples for this study. K. Deng thanks the China Scholarship Council (CSC) for a fellowship. We are also grateful to Professor C. Allen's group for providing us with access to their DSC apparatus.

## Appendix. Supporting information

The calculation of adhesion energies from lap shear test data. The supplementary data associated with this article can be found in the on-line version at, doi:10.1016/j.polymer.2009.04.079.

## References

[1] Lin YS, Yasuda HK. J Appl Polym Sci 1998;67:855–63.
[2] Yin Z, Yang J, Coombs N, Winnik MA, Ryntz RA, Yaneff PV. Polymer 2007;48:1297–305.
[3] Seki M, Vchida H, Maeda Y, Yamauchi S, Takgi K, Ukai Y, et al. Macromolecules 2000;33:9712–9.
[4] Yokoyama Y, Ricco T. Polymer 1998;39(16):3675–81.
[5] Mencik Z, Fitchmun DR. J Polym Sci Part B Polym Phys 1973;11:973–89.
[6] Tang H, Matin DC. J Mater Sci 2002;37:4777–85.
[7] Matsumoto K, Miura I, Hayashida K. Kobunshi Konbunshu 1979;36:401–6.
[8] Fujiyama M, Wakino T. J Appl Polym Sci 1991;43:57–81.
[9] Fujiyama M, Wakino T. J Appl Polym Sci 1988;35:29–49.
[10] Ryntz RA, McNeight A, Ford A. Plastic Eng 1996;52(9):35–8.
[11] Pennington BD, Ryntz RA, Urban MW. Polymer 1999;40:4795–803.
[12] Moffitt M, Rharbi Y, Li HX, Winnik MW. Macromolecules 2002;35:3321–4.
[13] Mirabella FM, Dioh N. Polym Eng Sci 2000;40:2000–6.
[14] Tomasetti E, Legras R, Henri-Mazeaud, Nysten B. Polymer 2000;41:6597–602.
[15] Ryntz RA, Xie Q, Ramamurthy AC. J Coat Technol 1995;67(840):35–46.
[16] Prater TJ, Karberline SL, Holubka JW, Ryntz RA. J Coat Technol 1996;68(857):83–91.
[17] Ryntz RA. Prog Org Coat 1996;27:241–54.
[18] Aoki Y. J Polym Sci Part C 1968;23:855.
[19] Morris HR, Munroe B, Ryntz RA, Treado PJ. Langmuir 1998;14:2426–34.
[20] Morris HR, Turner JF, Munroe B, Ryntz RA, Treado PJ. Langmuir 1999;15:2961–72.
[21] Ma YCh, Farinha JPS, Winnik MA. Macromolecules 2004;37:6544–52.
[22] Krotil HU, Stifter T, Waschipky H, Weishaupt K, Hild S, Marti O. Surf Interface Anal 1999;27:336–40.
[23] Rosa-Zeiser A, Weilandt E, Hild S, Marti O. Meas Sci Technol 1997;8:1333–8.
[24] Zhang H, Grim PCM, Foubert P, Vosch T, Vanoppen P, Wiesler UM, et al. Langmuir 2000;16:9009–14.
[25] Csete M, Kokavecz J, Bor Zs, Marti O. Mater Sci Eng C 2003;23:939–44.
[26] Risio SD, Yan N. Colloids Surf A Physicochem Eng Aspects 2006; 206, 289, 65–74.
[27] Boivin KC, Barry CMF, Orroth SA. SPE ANTEC'99 conference proceedings, 1999;3:3157–61.
[28] Russ JC. The image processing handbook. 4th ed. Boca Raton, Florida: CRC Press LLC; 2002.
[29] Rasband W. ImageJ, http://rsb.info.nih.gov/ij/, National Institute of Health, USA.
[30] Brandrup J, Immergut EH, editors. Polymer handbook. 3rd ed. New York: Wiley; 1989. V19, V29.
[31] Yin Z, Ma Y, Chen W, Coombs N, Winnik MA, Ryntz RA, et al. Polymer 2005;46:11610–23.
[32] Ellis TS. Polym Eng Sci 2001;41:2065–72.